Phonon-assisted oscillatory exciton dynamics in monolayer $MoSe_2$: Supplementary discussion

Colin M. Chow[1]*, Hongyi Yu[2]*, Aaron M. Jones[1], John R. Schaibley[3], Michael Koehler[4], David G. Mandrus[4,5], R. Merlin[6], Wang Yao[2†], Xiaodong Xu[1,7†]

This supplementary document is comprised of six sections: (i) PL lineshape fitting, (ii) exciton rise time and lifetime extraction, (iii) exciton and trion decay rates in time-resolved luminescence, (iv) exciton and trion steady-state dynamics, (v) data from a second monolayer $MoSe_2$ sample, and (vi) Raman spectrum from a third monolayer $MoSe_2$ sample. To simplify referencing, all labels for figures and tables in the Supplementary Discussion begin with the letter "S".

I. PL lineshape fitting

The PL lineshapes of both neutral exciton (X^0) and trion (X^-) are found to be inhomogeneously broadened in such a way that the broadening is on the same order of magnitude as the natural linewidth. Therefore, neither Lorentzian nor Gaussian lineshapes adequately fit the spectra, as shown in Fig. S1a. The shortcoming of these lineshapes is most evident in the "wings" of the resonances, where the best-fit Lorentzian curve overestimates the signal while the Gaussian curve underestimates it. As mentioned in the main text, we fit the spectra with Voigt profiles, or the plasma dispersion functions. Explicitly, the Voigt profile, $V(\omega;\omega_0,\sigma,\gamma)$, is given by the convolution between a Gaussian curve, $G(\omega;\sigma)$, and a Lorentzian curve, $L(\omega;\gamma)$:

$$V(\omega;\omega_0,\sigma,\gamma_0) = A\int_{-\infty}^{\infty} G(\omega'-\omega_0;\sigma)\,L(\omega-\omega';\gamma_0)d\omega',$$
$$G(\omega;\sigma) = \frac{1}{\sigma\sqrt{2\pi}}\exp(-\omega^2/2\sigma^2),$$
$$L(\omega;\gamma_0) = \frac{\gamma_0}{\pi(\omega^2+\gamma_0^2)}.$$

Here, A is a proportionality constant, ω_0 and σ the average (centre) and standard of deviation of the normally (Gaussian) distributed resonance, respectively, and γ_0 the half width at half maximum (HWHM) of the Lorentzian. For every PL spectrum, two separate sets of fitting parameters, A, ω_0, σ, and γ_0 are needed for the X^- and X^0 resonances. Fitting is accomplished by minimizing the squared error by performing multivariable nonlinear regression. Some spectra feature prominent narrow lines attributed to resonant Raman scattering. These are fitted manually with Gaussian curves. Since the linewidths of these narrow features are much less than that of X^- and X^0, their presence has minimal impact on the accuracy of the Voigt profile fits. As an example, the full-spectrum fit of Fig. 2b in the main text is shown in Fig. S1a below, along with fits using Lorentzian and Gaussian curves. The excellent fits produced with Voigt profiles for both X^- and X^0 resonances justify their use.

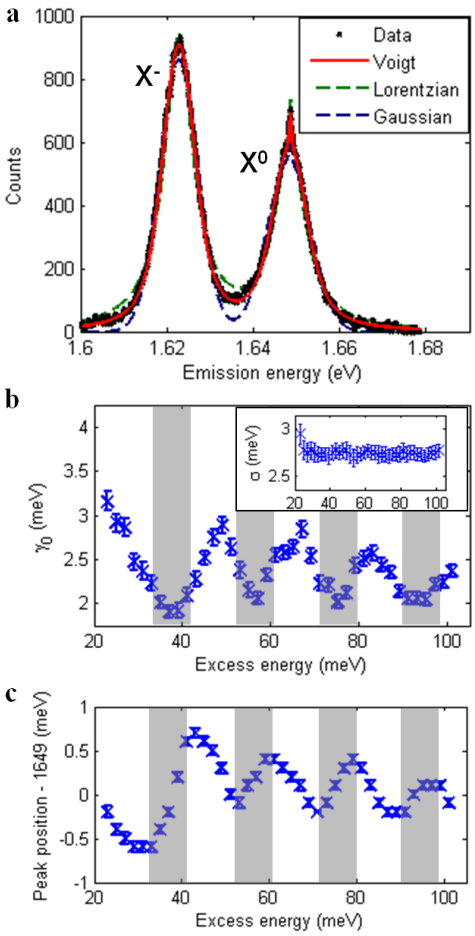

Fig. S1 **a** Full spectrum of Fig. 2b in the main text showing lineshape fits with Voigt, Lorentzian and Gaussian profiles, for both X^- and X^0 resonances. **b** Same as Fig. 4a in the main text, reproduced here for convenience: best-fit γ_0 of the X^0 resonance. **c** The centre of the X^0 resonance as a function of excess energy. Shaded regions indicate regions of enhanced luminescence obtained from Fig. 1b. Error bars represent 99% confidence intervals, defined as ±2.58 × standard error of fitted parameter.

[1]Department of Physics, University of Washington, Seattle, Washington 98195, USA. [2]Department of Physics and Center of Theoretical and Computational Physics, University of Hong Kong, Hong Kong, China. [3]Department of Physics, University of Arizona, Tuscon, Arizona 85721, USA. [4]Department of Materials Science and Engineering, University of Tennessee, Knoxville, Tennessee 37996, USA. [5]Materials Science and Technology Division, Oak Ridge National Laboratory, Oak Ridge, Tennessee 37831, USA. [6]Center for Photonics and Multiscale Nanomaterials and Department of Physics, University of Michigan, Ann Arbor, MI 48109, USA. [7]Department of Materials Science and Engineering, University of Washington, Seattle, Washington 98195, USA.
*These authors contributed equally to this work.
[†]Correspondence: Wang Yao (wangyao@hku.hk), Xiaodong Xu (xuxd@uw.edu)

The best-fit values of the fitting parameters are given in Table S1. Interestingly, the best-fit γ_0 and ω_0 for X^0 vary in an oscillatory manner with respect to the excitation photon energy, whereas those of X^- remain relatively constant. As shown in Fig. S1b, γ_0 of X^0 is reduced when the excitation laser is on a phonon resonance. Surprisingly, Fig. S1c reveals that ω_0 also oscillates with a period corresponding to the LA(M) phonon mode. However, the oscillations are not in phase with that of γ_0 because here the rising edges coincide with the phonon resonances. Artifacts from fitting can be ruled out with further analysis of the fitting error, e. g. from the lack of corresponding oscillations in the residue. The amplitude of oscillations roughly equals that of γ_0, but much smaller than the average homogeneous linewidth. This might be related to the oscillations of γ_0, in which efficient hot exciton relaxation and the subsequent smaller phonon bath is conjectured to prolong radiative lifetime (Section IV), hence reducing γ_0, with on-phonon-resonance excitation. Nonetheless, the physical mechanism behind the modulation of exciton resonance seen here remains to be explored.

Resonance	Parameter	Best-fit value (meV)
X^-	γ_0	2.30 ± 0.05
	σ	2.80 ± 0.05
	ω_0	1622.4 ± 0.1
X^0	γ_0	Varies. See Fig. S1b
	σ	2.80 ± 0.05
	ω_0	Varies. See Fig. S1c

Table S1 Best fit parameter values for both X^- and X^0 transitions. With the exception of γ_0 and ω_0 for the X^0 transition, all other parameters given here are found to vary only slightly with respect to the excitation energy, and without a clear oscillatory feature.

II. Exciton rise time and lifetime extraction

In time-resolved PLE measurements, due to the finite response time of the streak camera, the output is the convolution of the time-dependent emission with the instrument response function, IRF. Since the timescale of $MoSe_2$ exciton dynamics is in the picosecond range, on the same order of magnitude as the nominal resolution (1 ps) of the streak camera, the measured time evolution of the emission will be noticeably stretched by about 1 ps. To obtain more accurate timing parameters, we perform deconvolution on the streak camera output with linear least-squares regression[1]. By scattering light from a mode-locked Ti-Sapphire laser with 150 fs pulse width into the streak camera, we measured a 1.5 ps full-width-at-half-maximum (FWHM) response. This is shown in Fig. S2a (dotted line) and taken as the IRF for deconvolution. To avoid overfitting and to improve numerical stability of the deconvolution protocol, Tikhonov regularization[1] is applied. With an appropriate choice of Tikhonov factor, the noise in the reconstructed temporal profile can be suppressed without affecting the overall response, as exemplified by the time traces of the trion emission, before (dashed line) and after (solid line) deconvolution, in Fig. S2a. The same deconvolution procedure is applied to all streak camera images taken at different excitation frequencies. Expectedly, we find that the rise times of

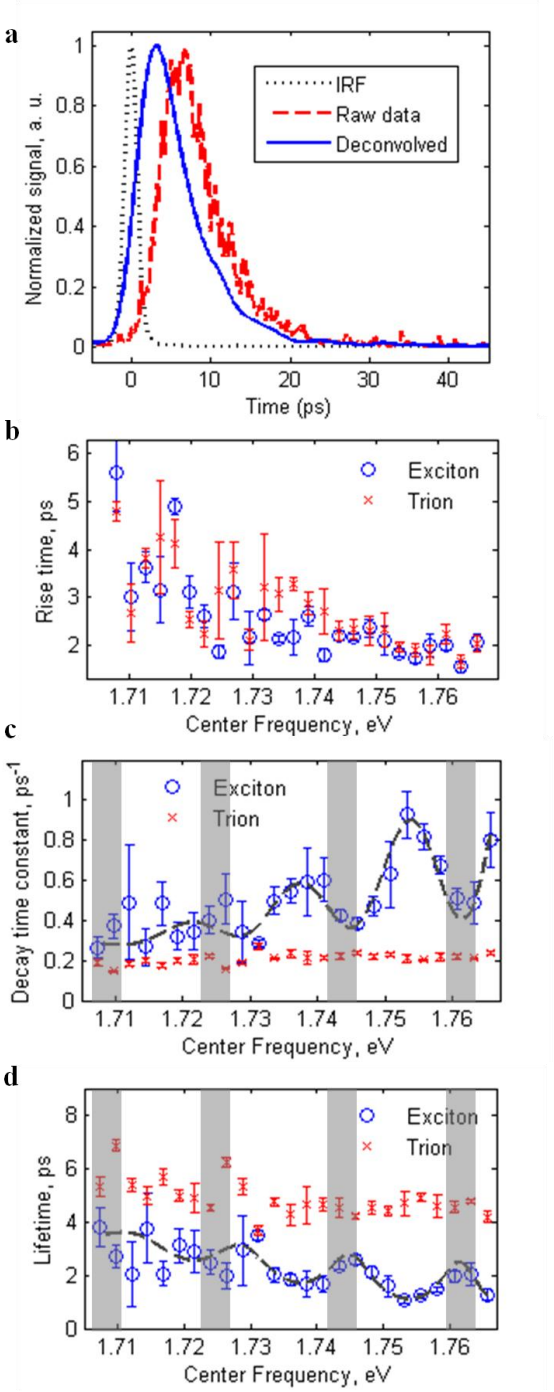

Fig. S2 **a** Vertical time traces of trion emission from Fig. 4b. Red dashed curve is the raw streak camera measurement while blue solid curve the deconvolved data, with the IRF represented by the dotted line. **b** Excitation frequency-dependent rise times of X^- (crosses) and X^0 (circles) emission extracted from a series of streak camera measurements in varying excitation energy. Error bars represent the standard deviations. **c** Excitation frequency-dependent decay rate, γ, of X^- (crosses) and X^0 (circles). **d** Same data as in **c**, presented as the lifetime, τ. Reproduced from Fig. 4e.

X^0 and X^- emission are reduced by roughly 1 ps following deconvolution, as compared with those extracted from the raw data. Nonetheless, their variations with respect to excitation frequency remain qualitatively similar with or without deconvolution.

From the deconvolved data, we obtain the rise times and lifetimes of X^0 and X^- with respect to excitation energy as presented in Fig. S2b – d. The rise time is simply defined as the time interval for which the rising edge of the luminescence moves from 10% to 90% of peak emission. To obtain the decay rate, a linear fit to the logarithm of the falling edge is applied, where the slope gives the decay time constant, γ. The extracted excitation dependent decay rates for the first sample is shown in Fig. S2c. To facilitate comparison with the rise time, the data in the main text is presented as the lifetime, $\tau = 1/\gamma$. For the conversion of the error bars from $\varepsilon(\gamma)$ to $\varepsilon(\tau)$, the first order approximation $\varepsilon(\tau) = \varepsilon(\gamma)/\bar{\gamma}^2$ is adopted, where $\bar{\gamma}$ denotes the mean value of γ. The result of the conversion is reproduced here in Fig. S2d.

III. Exciton and trion decay rates in time-resolved luminescence

The exciton dispersion curve is shown in Fig. S3a, where only excitons inside the light cone ($k \le \omega_{X^0}/c$) can radiatively recombine. To model the exciton decay process, we consider a simplified three-level system as shown in Fig. S3b. $|D\rangle$ represents the dark exciton state outside the light cone ($k > \omega_{X^0}/c$), with time dependent density $N_D(t)$, which nonradiatively decays to the vacuum state $|0\rangle$ with a rate Γ_{nr}. $|B\rangle$ is the bright exciton state inside the light cone ($k \le \omega_{X^0}/c$), with time-dependent density $N_B(t)$, which decays to $|0\rangle$, both radiatively and nonradiatively, with a total rate $\Gamma_t = \Gamma_{nr} + \Gamma_r$. The nonradiative decay rate includes relaxation from excitons to trions. Scattering with other excitons, free carriers, impurities, and long-wavelength (small k) phonons can induce interconversion from $|D\rangle$ to $|B\rangle$ and vice versa, with the corresponding rates given by γ_1 and γ_2, respectively. Given the ~meV linewidth of excitons inside the light cone[2], interconversion from $|D\rangle$ to $|B\rangle$ can be induced by both phonon emission and absorption, whose coupling matrix elements are proportional to $\sqrt{N_{\mathbf{k}}+1}$ and $\sqrt{N_{\mathbf{k}}}$, respectively, where $N_{\mathbf{k}}$ is the number of **k**-vector phonon. Consequentially, γ_1 and γ_2 increase with $N_{\mathbf{k}}$.

$N_B(t)$ and $N_D(t)$ are governed by the coupled rate equations

$$\frac{d}{dt}N_B = -(\Gamma_t + \gamma_2)N_B + \gamma_1 N_D,$$
$$\frac{d}{dt}N_D = \gamma_2 N_B - (\Gamma_{nr} + \gamma_1)N_D.$$

Solving the above rate equations, we find

$$N_B(t) = Ae^{-x_f t} + Be^{-x_s t},$$
$$N_D(t) = A'e^{-x_f t} + B'e^{-x_s t},$$

where A, B, A' and B' are time-independent constants determined by the initial values $N_{B,D}(0)$. The PL emission rate is given by $\Gamma_r N_B(t)$, which has two decay time constants, x_f and x_s. Under a low temperature we can take[3] $\Gamma_r \sim 3\ \mathrm{ps}^{-1} \gg \gamma_1$ such that $(\Gamma_r + \gamma_2 - \gamma_1)^2 \gg 4\gamma_1\gamma_2$, the fast (slow) decay constant x_f (x_s) is then given by

$$x_f = \frac{\Gamma_t+\gamma_2+\Gamma_{nr}+\gamma_1}{2} + \sqrt{\left(\frac{\Gamma_t-\Gamma_{nr}+\gamma_2-\gamma_1}{2}\right)^2 + \gamma_1\gamma_2} \approx \Gamma_t + \gamma_2.$$
$$x_s = \frac{\Gamma_t+\gamma_2+\Gamma_{nr}+\gamma_1}{2} - \sqrt{\left(\frac{\Gamma_t-\Gamma_{nr}+\gamma_2-\gamma_1}{2}\right)^2 + \gamma_1\gamma_2} \approx \Gamma_{nr} + \gamma_1.$$

Now x_f corresponds to the total decay rate of the bright excitons inside the light cone, and x_s that of the dark excitons outside the light cone.

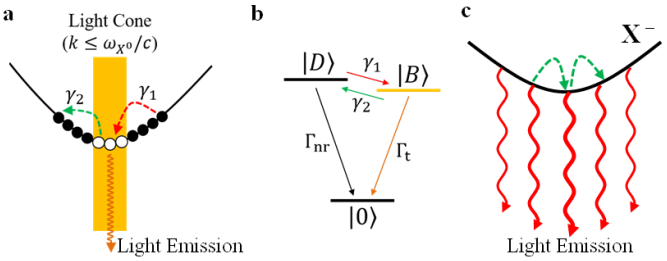

Fig. S3 **a** Dispersion relation of neutral exciton, where the horizontal axis represents center-of-mass momentum. The light cone (yellow region) corresponds to center-of-mass wavevector, $k \le \omega_{X^0}/c$, in which excitons are bright and can radiatively recombine (wavy arrow). Excitons outside the light cone are optically dark. Interconversion between bright and dark excitons (dashed arrows) can occur via scattering. **b** Three level model for neutral excitons, with relaxation rates indicated. $|D\rangle$: dark exciton, $|B\rangle$: bright exciton, $|0\rangle$: vacuum state. **c** Dispersion relation of the trion (solid black curve) and its radiative decay (red wavy arrows). Unlike the exciton, the radiative decay rate of the trion varies slowly with **k**, such that the scattering induced by long-wavelength phonons (green curved arrows) barely changes the overall decay rate. The thickness of the wavy arrows illustrates varying decay rate with respect to wavevector.

Theory has shown that bright excitons in monolayer TMDs have a very short radiative lifetime[3], as evidenced by the measured decay rate[2,4] of $x_f \sim 3\ \mathrm{ps}^{-1}$. This value is significantly larger than the inverse of PL rise time (0.2 – 1 ps^{-1}) and decay rate (0.2 – 1 ps^{-1}) shown in Fig. S2b and c. Possibly, in our time-resolved measurements, by the time the recorded luminescence intensity reaches its maximum, the bright exciton density inside the light cone is depleted. The luminescence detected at a later time predominantly comes from scattering-induced dark-to-bright exciton conversion, whose decay rate is given by $x_s \approx \Gamma_{nr} + \gamma_1 \sim 0.2 - 1\ \mathrm{ps}^{-1}$. The variation of PL decay time (x_s^{-1}) mainly comes from the modulation of the scattering rate, γ_1, which increases with the density of long-wavelength phonons. A related behavior due to the weak scattering rate at low temperature, termed "exciton-phonon relaxation bottleneck", has also been discussed in a recent paper[5].

In contrast to the exciton, trion has rather different radiative properties[3]. In particular, a trion with large momentum can radiatively decay, as the momentum conservation can be satisfied with the left-behind electron inherits the trion wavevector (the electron recoil effect[6]). The radiative decay rate varies slowly with the trion wavevector[3], such that scattering with long wavelength-phonons barely changes the overall decay rate of the trion (see Fig. S3c). Therefore, unlike the exciton, trion does not show lifetime oscillation with the excitation energy.

IV. Exciton and trion steady-state dynamics

The contrasting behaviors of exciton and trion luminescence in PLE with excitation energy can be explained by their distinct radiative properties. For the excitons, momentum conservation allows only those inside the narrow light cone ($k \leq \omega_{X^0}/c \sim 10^{-3}$ Å^{-1}) to radiatively recombine. These bright excitons have an ultrafast radiative decay rate[3] of about 3 ps^{-1}. On the other hand, trions in a much larger momentum range can radiatively recombine, with a smoothly changing decay rate[3,6].

The PLE spectra are determined by the steady-state population distribution of excitons/trions. We expect the steady-state total exciton/trion population to depend weakly on the excitation energy because: (i) on- or off-phonon resonance affects only the kinetic energy of the generated exciton, while the generation rate is nearly unaffected as it is determined by the LA(M) phonon emission rate; (ii) most of the trions are the outcome of subsequent relaxation from excitons[7] which is insensitive to the exciton kinetic energy (rather, trion formation rate is mostly determined by phonon emission rates of A_1' and other optical phonons[8]).

Nonetheless, the excitation energy strongly affects the exciton population distribution in *k*-space. When the excitation is off-phonon resonance, it generates excitons with a finite kinetic energy, resulting in excitons with a wide steady-state *k*-space distribution (see Fig. S4a). A large number of excitons have high energies, and cannot be efficiently scattered into the light cone for radiative recombination due to energy conservation. On the other hand, when the excitation is on-phonon resonance, it generates excitons with close to zero kinetic energy. The subsequent exciton steady-state *k*-space distribution is narrower (Fig. S4b). When the excitation laser is tuned across phonon resonances, the variation of exciton distribution in *k*-space leads to the observed oscillations in PLE luminescence spectra.

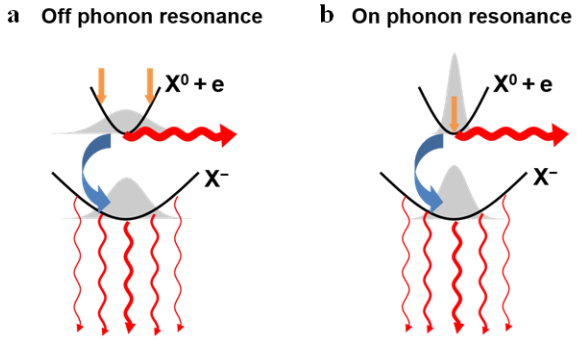

Fig. S4 Exciton and trion steady-state *k*-space distributions for **a** on- and **b** off-phonon-resonance excitation. The upper parabola represents the dispersion curve of an exciton together with a free electron (X^0 + e), while the lower that of a trion (X^-). Orange arrows indicate laser generated exciton energies following phonon emission (see Fig. 5b & c in the main text), while blue curved arrows illustrate the relaxation process from a neutral exciton to a trion. Red wavy arrows represent the radiative decay process, whose thickness corresponds to the wavevector-dependent decay rate. Only excitons lying in the vicinity of valley extremum can radiatively recombine, while all trions can radiatively recombine with a slowly changing decay rate. Shaded Gaussian curves correspond to the exciton and trion *k*-space distributions.

Most trions are formed via the relaxation of excitons[7]. This additional step can partially reduce the difference of trion *k*-space distributions between exciting on- and off-phonon resonance. Meanwhile, trions in a much larger momentum range can radiatively decay with a slowly changing decay rate (Fig. S4). This further diminishes the variation of trion emission as a function of excitation energy.

V. Data from a second monolayer $MoSe_2$ sample.

Data from a second monolayer $MoSe_2$ sample (Fig. S5a) exfoliated from a different bulk crystal is presented in Fig. S5b – g. In this sample, the resonances for both X^- and X^0 are blue-shifted by about 3 meV relative to the first sample. Nonetheless, the phonon resonances are identical (within the uncertainty of 1 meV) to those found in the first sample, as can be seen in the vertical line cut at the X^0 resonance shown in Fig. S5c. Here, we have included additional Raman peak assignments in addition to the LA(M) overtones where space allows. These assignments are provisional, especially for higher order modes, because multiple phonon combinations may give rise to the same energy.

The emission lineshapes of X^0 and X^- in the second monolayer $MoSe_2$ is different from those in the first in the sense that they are slightly asymmetric. As a result, fitting using two Voigt profiles as is done in the previous case becomes inadequate here. Nonetheless, we found that excellent fits can be produced by adding two Gaussian curves whose peak positions and widths are constant, i.e., independent of the excitation energy, as shown in Fig. S5d. Their peak positions are each about 10 meV lower than X^0 and X^- resonances. Given their large linewidths of about 7.5 meV, they are unlike to be originating from defect states. It is more likely that their presence is due to contamination or inhomogeneity as a result of lattice distortion. Despite this, HWHM of X^0 emission, γ_0, extracted from the lineshape analysis shows oscillations with a period close to the LA(M) phonon mode (Fig. S5e), as is the case in the first sample. However, oscillations are also noticeable in the inhomogeneous broadening width, σ, as shown in the inset of Fig S5e, although the amplitude of oscillations (about 0.15 meV) is much smaller than that of γ_0. This is likely an artifact of the fit due to the weaker X^0 emission intensity and the more pronounced Raman scattering components present in the second sample. Regardless, the oscillatory behavior of the homogeneous linewidth and of the peaks position of X^0 (Fig. S5f) qualitatively agrees with results obtained from the first sample.

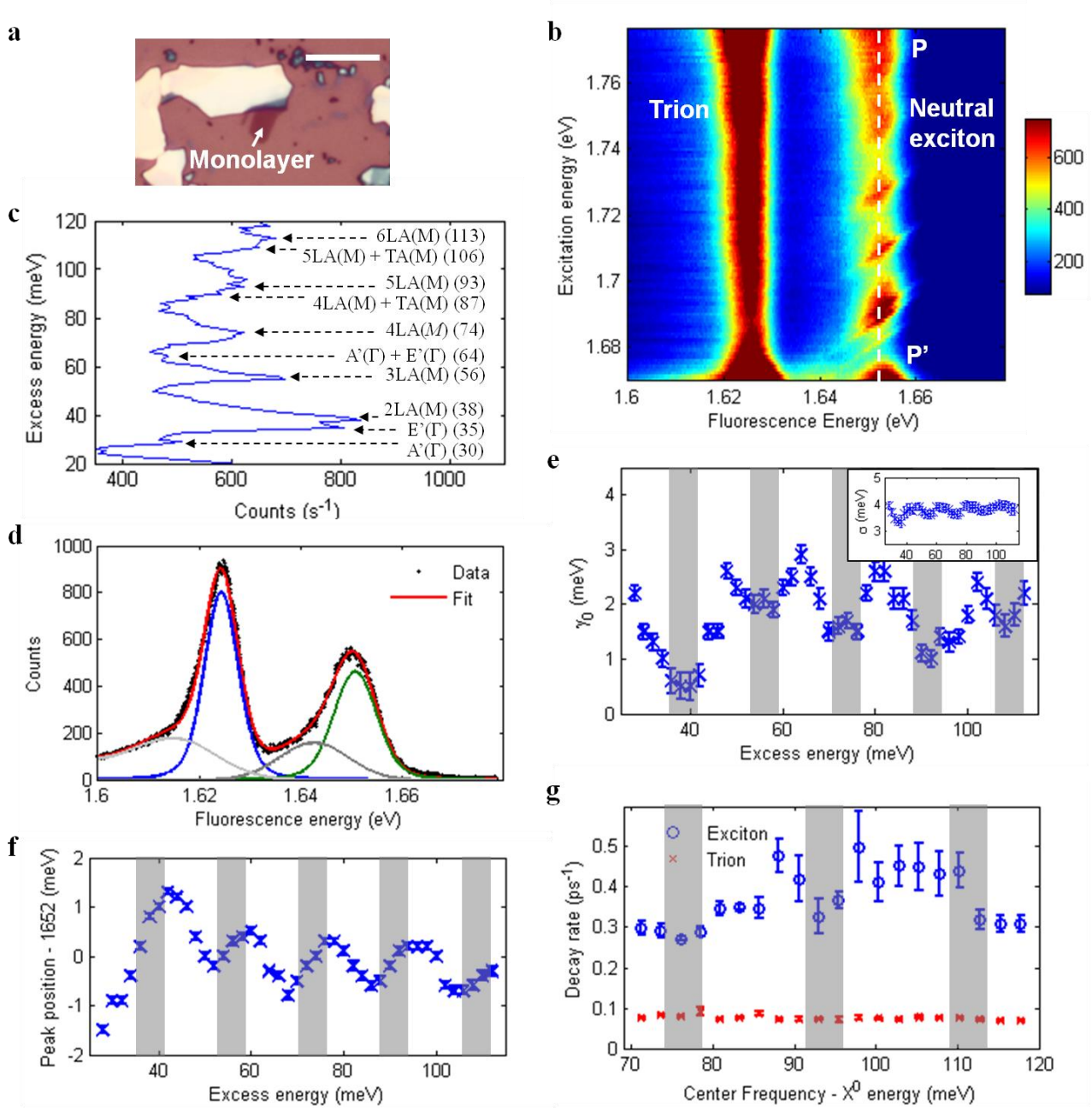

Fig. S5 **a** Optical micrograph of a second monolayer $MoSe_2$. Scale bar: 10 μm. **b** PLE spectra of the second sample, showing neutral exciton and trion emission centered at 1.653 eV and 1.626 eV, respectively. Colour bar: counts per second. **c** Vertical line cut P – P' of the PLE spectra shown in **b** with selected phonon peaks marked by arrows. **d** An example of the PL emission spectra with fit. Solid black circles are data points while the solid red line is the fit constructed from the following components: Voigt profiles for trion (solid blue line) and neutral exciton (solid greed line), and the Gaussian background (solid dark and light grey). **e** Best-fit homogeneous linewidth, γ_0, of the X^0 resonance as a function of excess energy extracted from lineshape analysis of the PLE intensity map in **b**. Inset: Width of the inhomogeneous (Gaussian) broadening, σ. **f** Peak position of the X^0 resonance as a function of excess energy. Error bars in both **e** and **f** represent 99% confidence intervals of the fits, while shaded regions correspond to regions of enhanced luminescence seen in **b**. **g** Excitation frequency-dependent decay rates, γ's, of X^- (crosses) and X^0 (circles) extracted by fitting the exponential decay time of the emission.

VI. Raman spectrum of a third monolayer $MoSe_2$ sample

Raman spectrum of a third monolayer $MoSe_2$ sample is shown in Fig. S6 below. The spectrum is taken at room temperature, with an excitation laser wavelength and intensity of 514 nm and 2 mW, respectively. The resonances observed agree with the spectra obtained by other groups[9–11], as well as our PLE data shown in Fig. 2c in the main text. The linewidths of the prominent peaks, e. g. A_1' and E', are found to range from 0.5 to 1 meV, matching those in the PLE spectra.

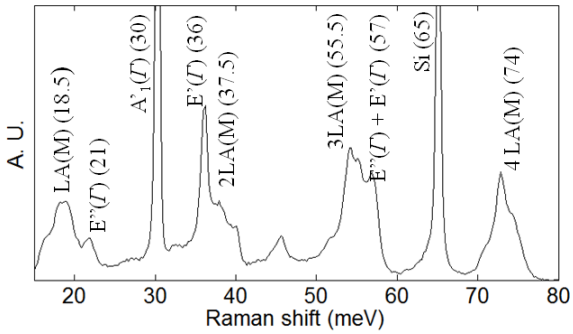

Fig. S6 Raman spectrum of a third monolayer $MoSe_2$ sample. Prominent peaks are labeled with corresponding phonon modes, along with the Raman shifts (in units of meV) in parentheses.

REFERENCES

1. Hansen, P. C. Regularization tools: a Matlab package for analysis and solution of discrete ill-posed problems. *Numer. Algorithms* **6,** 1–35 (1994).
2. Hao, K. *et al.* Coherent and Incoherent Coupling Dynamics between Neutral and Charged Excitons in Monolayer $MoSe_2$. *Nano Lett.* **16,** 5109–5113 (2016).
3. Wang, H. *et al.* Radiative lifetimes of excitons and trions in monolayers of the metal dichalcogenide MoS_2. *Phys. Rev. B* **93,** 45407 (2016).
4. Poellmann, C. *et al.* Resonant internal quantum transitions and femtosecond radiative decay of excitons in monolayer WSe_2. *Nat. Mater.* **14,** 889–893 (2015).
5. Slobodeniuk, A. O. & Basko, D. M. Exciton-phonon relaxation bottleneck and radiative decay of thermal exciton reservoir in two-dimensional materials. *Phys. Rev. B* **94,** 205423 (2016).
6. Ross, J. S. *et al.* Electrical control of neutral and charged excitons in a monolayer semiconductor. *Nat. Commun.* **4,** 1474 (2013).
7. Singh, A. *et al.* Trion formation dynamics in monolayer transition metal dichalcogenides. *Phys. Rev. B* **93,** 41401 (2016).
8. Jones, A. M. *et al.* Excitonic luminescence upconversion in a two-dimensional semiconductor. *Nat. Phys.* **12,** 323–327 (2016).
9. Zhang, M. *et al.* Two-dimensional molybdenum tungsten diselenide alloys: photoluminescence, Raman scattering, and electrical transport. *ACS Nano* **8,** 7130–7137 (2014).
10. Zhang, X. *et al.* Phonon and Raman scattering of two-dimensional transition metal dichalcogenides from monolayer, multilayer to bulk material. *Chem. Soc. Rev.* **44,** 2757–2785 (2015).
11. Soubelet, P., Bruchhausen, A. E., Fainstein, A., Nogajewski, K. & Faugeras, C. Resonance effects in the Raman scattering of monolayer and few-layer $MoSe_2$. *Phys. Rev. B* **93,** 155407 (2016).